









Absence of long-range magnetic order in $\text{Fe}_{1-\delta}\text{Te}_2$ ($\delta \approx 0.1$) crystals

Jianjun Tian (田建军) ^{1,2,*}, V. N. Ivanovski ³, M. Abeykoon,⁴ R. M. Martin,⁵ S. Baranets ⁶, C. Martin ⁷,
 Yu Liu (刘育) ^{1,†}, Qianheng Du (杜乾衡),^{1,8,‡} Aifeng Wang (王爱峰),⁹ Shuzhang Chen (陈淑彰),^{1,10} Xiao Tong (佟晓),¹¹
 Weifeng Zhang (张伟风),² S. Bobev ⁶, V. Koteski ³ and C. Petrovic ^{1,8,10,§}

¹Condensed Matter Physics and Materials Science Department, Brookhaven National Laboratory, Upton, New York 11973, USA

²Research Center of Topological Functional Materials and Henan Key Laboratory of Photovoltaic Materials, Henan University, Kaifeng 475004, China

³Department of Nuclear and Plasma Physics, Vinca Institute of Nuclear Sciences, National Institute of the Republic of Serbia, University of Belgrade, 11001 Belgrade, Serbia

⁴Photon Science Division, National Synchrotron Light Source II, Brookhaven National Laboratory, Upton, New York 11973, USA

⁵Department of Physics and Astronomy, Montclair State University, Montclair, New Jersey 07043, USA

⁶Department of Chemistry and Biochemistry, University of Delaware, Newark, Delaware 19716, USA

⁷School of Theoretical and Applied Sciences, Ramapo College of New Jersey, Mahwah, New Jersey 07430, USA

⁸Department of Materials Science and Chemical Engineering, Stony Brook University, Stony Brook, New York 11790, USA

⁹School of Physics, Chongqing University, Chongqing 400044, China

¹⁰Department of Physics and Astronomy, Stony Brook University, Stony Brook, New York 11794-3800, USA

¹¹Center of Functional Nanomaterials, Brookhaven National Laboratory, Upton, New York 11973, USA



(Received 26 February 2021; revised 18 October 2021; accepted 1 December 2021; published 27 December 2021)

Transition metal dichalcogenides attract considerable attention due to a variety of interesting properties, including long-range magnetism in nanocrystals. Here we investigate the magnetic, thermal, and electrical properties of an FeTe_2 single crystal with iron vacancy defects. Magnetic measurements show a paramagnetic state and the absence of magnetic order with low anisotropy in the magnetic susceptibility. Fe $3d$ orbitals are well hybridized, contributing to the bad metal electrical resistivity. Observed thermal conductivity values below room temperature are rather low and comparable to those of high-performance thermoelectric materials. Our results indicate that FeTe_2 can form in a highly defective marcasite crystal structure which can be exploited in future materials design.

DOI: [10.1103/PhysRevB.104.224109](https://doi.org/10.1103/PhysRevB.104.224109)

I. INTRODUCTION

Transition metal dichalcogenides have been widely investigated for their rich physical properties and for potential applications such as spintronics, catalysis, batteries, and photodetectors [1–5]. Some transition metal ditellurides such as FeTe_2 adopt three-dimensional marcasite- or pyrite-type structures without a van der Waals (vdW) gap in the crystal structure [6,7]. Marcasite-type FeTe_2 crystallizes in the $Pn\bar{m}$ space group, and it has been characterized as a magnetic semiconductor of interest for thermoelectric applications [7–13]. The ferromagnetic state was predicted to persist in monolayers [14–16]; however, disordered ultrathin nanocrystals of mixed marcasite and hexagonal FeTe_2 showed no signature of magnetic order down to 2 K [17,18].

On the other hand, it is known that defects and imperfections can tune properties of semiconductors [19]. Defects might also suppress [20] or enhance long-range magnetic order [21]. Whereas the stoichiometry of FeTe_2 has not been evaluated in great detail so far, a possible width of formation for orthorhombic iron telluride with the approximate stoichiometry of $\text{FeTe}_{2.0}$ was noted [22], suggesting a possible deviation from full occupancy on the Fe atomic site. Therefore, it is of interest to study the influence of crystal imperfections on the physical properties of iron ditelluride. They are best studied in single crystals amenable for a variety of experimental probes.

Here we report the absence of magnetic order in FeTe_2 crystals with vacancy defects down to 2 K and bad metal behavior with low anisotropy at scattering rates of $1/\tau$. By using combined first-principles calculations and average and local crystal structure studies we find that vacancy defects reside primarily on Fe atoms, without breaking the average and local crystal symmetries of the marcasite-type $Pn\bar{m}$ space group. This results in an $\text{Fe}_{1-\delta}\text{Te}_2$ stoichiometry with $\delta = 0.10(6)$ and rather low values of thermal conductivity at and below room temperature. The relatively high tolerance for Fe defects calls for a detailed study of the stoichiometry in ultrathin crystals of transition metal ditellurides and the induced properties.

* tjj@henu.edu.cn

[†]Present address: Los Alamos National Laboratory, MS K764, Los Alamos, New Mexico 87545, USA.

[‡]Present address: Materials Science Division, Argonne National Laboratory, Lemont, Illinois 60439, USA.

[§]petrovic@bnl.gov

II. EXPERIMENTAL AND THEORETICAL DETAILS

Flux-grown single crystals of FeTe₂ were grown from excess Te with an Fe:Te = 1:10 mole ratio. The source elements were put into an alumina crucible sealed in a quartz tube with the partial pressure of argon gas. The heating temperature for the tube was ramped to 900 °C and then cooled to 450 °C over 100 h, at which time crystals were decanted from liquid. Long, needlelike single crystals up to 7 mm long along the *b* axis crystallized. Single crystals of FeTe₂ were also grown using chemical vapor transport (CVT). First, the FeTe₂ polycrystalline sample was made by heating a stoichiometric proportion of Fe and Te at 950 °C. Polycrystal powder was sealed with iodine in a quartz tube that was placed in a temperature gradient between 750 °C and 650 °C for 1 week. Single crystals up to 3 × 1 × 1 mm³ were grown.

Single-crystal x-ray intensity data sets were collected for two crystals from each preparation method. The crystals were selected under a microscope and cut to dimensions of 0.05 × 0.06 × 0.08 mm³ (CVT) and 0.04 × 0.07 × 0.08 mm³ (flux-grown crystals). The crystals were mounted on low background plastic holders using Paratone N oil, transferred to the goniometer, and placed under a cold stream of nitrogen gas (200 K). Data acquisitions took place on a Bruker Apex DUO diffractometer using graphite monochromatized Mo *K*α radiation ($\lambda = 0.71073$ Å). Approximately a quarter of the sphere of reciprocal space data was collected in each case (two batch runs at different ω and ϕ angles with an exposure time of 8 s/frame). A total of 2578 reflections were collected for CVT, and a total of 1495 reflections were collected for flux-grown crystal ($2\theta_{\max} = 60^\circ$), 248 and 224 of which were unique ($T_{\min}/T_{\max} = 0.223/0.313$, $R_{\text{int}} = 0.053$; $T_{\min}/T_{\max} = 0.219/0.384$, $R_{\text{int}} = 0.048$), respectively. The data collection, data reduction and integration, and refinement of the cell parameters were carried out using Bruker's software. Semiempirical absorption correction was applied with the aid of the SADABS software package. The structure was subsequently solved by direct methods and refined on F^2 (13 parameters) with the aid of the SHELXL package [23]. All atoms were refined with anisotropic displacement parameters with scattering factors (neutral atoms) and absorption coefficients [24].

Pair distribution function (PDF) and wide-angle x-ray scattering measurements were carried out in capillary transmission geometry using a Perkin Elmer amorphous silicon area detector at the 28-ID-1 (PDF) beamline of the National Synchrotron Light Source II at Brookhaven National Laboratory on flux-grown crystals. The setup utilized an ~74 keV ($\lambda = 0.16635$ Å) x-ray beam. Two-dimensional diffraction data were integrated using the FIT2D software package [25]. The data reduction was done to obtain experimental PDFs ($Q_{\max} = 26$ Å⁻¹) using the XPDFSUITE software package. The Rietveld and PDF analyses were carried out using GSAS-II and PDFGUI software packages, respectively [26,27].

Electrical and thermal transport, heat capacity, and magnetic measurements were carried out with Quantum Design PPMS-9 and MPMS-XL5. The thermal gradient and current direction were applied along the *b* axis in the thermal and electrical transport measurements, respectively. The average stoichiometry was determined by examining multiple

points on cleaved fresh surfaces and was checked by multiple samples from the same batch using energy-dispersive x-ray spectroscopy (EDX) in a JEOL LSM-6500 scanning electron microscope.

Reflectance between 300 cm⁻¹ (37 meV) and 50.000 cm⁻¹ (6.2 eV) was measured using a combination of two different instruments: a Bruker Vertex 70 FTIR (300 - 24.000) cm⁻¹ and a Perkin-Elmer 650 UV/VIS grating spectrometer (12.000 to 50.000) cm⁻¹. A single crystal with a mirrorlike face approximately 0.5 mm² in area with a nearly rectangular shape was measured with unpolarized light, as well as with polarization along the *a* and *b* axes of the crystal structure. Polarization measurements were performed between 300 and 20.000 cm⁻¹.

The measurements of the Mössbauer effect were performed in transmission geometry using a ⁵⁷Co(Rh) source at the room temperature. The sample mass was chosen to match the ideal Mössbauer thickness. The spectra were recorded in the low ($|v| < 2.05$ mm s⁻¹) and high ($|v| < 8.85$ mm s⁻¹) velocity ranges. The Voigt-function-based fitting (VBF) module incorporated in the RECOIL program was used to refine the measured spectra [28]. The Wissel spectrometer was calibrated using the spectrum of the natural iron foil. The center shift values are in reference to metallic alpha iron ($\delta = 0$). The low-velocity spectrum was also evaluated by means of the WINNORMOS-DIST program based on the histogram method [29].

The x-ray photoemission spectroscopy (XPS) was performed in ultrahigh vacuum, where base pressures was less than 2×10^{-9} Torr using a hemispherical electron energy analyzer (SPECS, PHOIBOS 100) and twin anode x-ray source (SPECS, XR50). Al *K*α (1486.7 eV) radiation was used at 10 kV and 30 mA. The angle between the analyzer and x-ray source is 45°, and photoelectrons were collected along the sample surface normal. For the XPS measurement, samples were prepared in a glove box and were transferred for measurement in a high-vacuum suitcase.

First-principles calculations were performed using the APW+LO method as implemented in the WIEN2K code [30]. A plane wave cutoff defined by $R_{\text{mt}}K_{\text{max}} = 8.0$ and sphere sizes of 2.1 a.u. (Fe) and 2.3 a.u. (Te) were used. The exchange-correlation potential was calculated by the generalized gradient approximation, using the scheme of Perdew, Burke, and Ernzerhof [31]. The core states were treated fully relativistically, while the valence states were treated within the scalar relativistic approximation. The threshold energy between valence and core states was -7 Ry in order to include low-lying Fe *s* states. The Brillouin zone (BZ) integrations within the self-consistency cycles were performed via a tetrahedron method, using 756 *k* points in the irreducible wedge of the BZ [32]. The lattice parameters throughout our calculations were fixed to their experimental values, and only the atomic positions were relaxed according to the Hellmann-Feynman forces calculated at the end of each self-consistent cycle.

III. RESULTS AND DISCUSSION

EDX analysis revealed that the ratio of Fe to Te in flux-grown crystals was Fe_{0.95(3)}Te₂, whereas in CVT-grown

TABLE I. Selected single-crystal data collection and structure refinement parameters for two independent iron ditelluride crystals using $\lambda = 0.71073 \text{ \AA}$ at 200 K. Here the “-f” and “-c” labels denote crystals grown from excess Te flux and by chemical vapor transport, respectively. The corresponding crystallographic information file (CIF) has been deposited with the Cambridge Crystallographic Database Centre [33].

	Refined composition	
	Fe ₂ -f	Fe ₂ -c
Formula weight (g/mol)	307.14	307.14
Space group	<i>Pnmm</i>	<i>Pnmm</i>
<i>Z</i>	2	2
<i>a</i> (Å)	5.2876(6)	5.2925(7)
<i>b</i> (Å)	6.2716(7)	6.2752(9)
<i>c</i> (Å)	3.8529(4)	3.8466(5)
<i>V</i> (Å ³)	127.77(2)	127.75(3)
Calculated density (g/cm ³)	7.98	7.98
$R_1 [I > 2\sigma(I)]^a$	0.019	0.018
$wR_2 [I > 2\sigma(I)]^a$	0.044	0.038
$\Delta\rho_{\text{max,min}}/e \text{ \AA}^{-3}$	1.66, -1.51	1.69, -1.22

$$^a R_1 = \frac{\sum |F_0| - |F_c|}{\sum |F_0|}, \quad wR_2 = \frac{[\sum (|F_0^2| - |F_c^2|)^2 / \sum (wF_0^2)^2]^{1/2}}{w},$$

$$w = 1/[\sigma^2 F_0^2 + (AP)^2] \quad [A = 0.0238 \text{ (Fe}_2\text{-c) and } A = 0.0127 \text{ (Fe}_2\text{-f)}; P = (F_0^2 + 2F_c^2)/3].$$

crystals it was Fe_{0.98(10)}Te₂, indicating possible Fe vacancy defects in both types of crystals. Single-crystal x-ray refinement (Table I) indicates that the final Fourier map is featureless with the highest residual density and deepest hole of about $1.6 e^-/\text{\AA}^3$, situated 0.8 and 0.7 Å away from Te, respectively. The occupancies of the Fe sites were set free for both data sets, both of which gave nearly identical deviations from unity, 0.928(5) for the former and 0.927(5) for the latter. Crystallographic data for the refinement shown in Tables I and II indicate that both flux- and CVT-grown crystals feature Fe atomic vacancies with negligible differences between the two types of crystals. All further analysis was performed on flux-grown crystals, although magnetic susceptibility was measured for both CVT- and flux-grown crystals. For further insight into Fe atomic vacancies, we performed Rietveld and PDF analyses of room temperature x-ray diffraction data [Figs. 1(a) and 1(b)]. A two-phase structural model that contains marcasite-type FeTe₂ [space group *Pnmm* (58)] and pure Te [space group *P3₁21* (152)] was re-

TABLE II. Atomic coordinates, displacements parameters U_{eq} (Å²), and the occupancy (occ.) of atomic sites for Fe_{1- δ} Te₂ refined from the single-crystal x-ray diffraction experiment at 200 K using $\lambda = 0.71073 \text{ \AA}$ in the single-crystal diffraction experiment. U_{eq} is defined as one third of trace of the orthogonalized $U_{i,j}$. The labels “-c” and “-f” denote CVT- and flux-grown crystals, respectively.

Atom	Site	<i>x</i>	<i>y</i>	<i>z</i>	U_{eq}	occ.
Fe-c	2a	0	0	0	0.006(1)	0.927(5)
Te-c	4g	0.22207(6)	0.36159(4)	0	0.006(1)	1.000
Fe-f	2a	0	0	0	0.007(1)	0.928(5)
Te-f	4g	0.22169(7)	0.36155(5)	0	0.007(1)	1.000

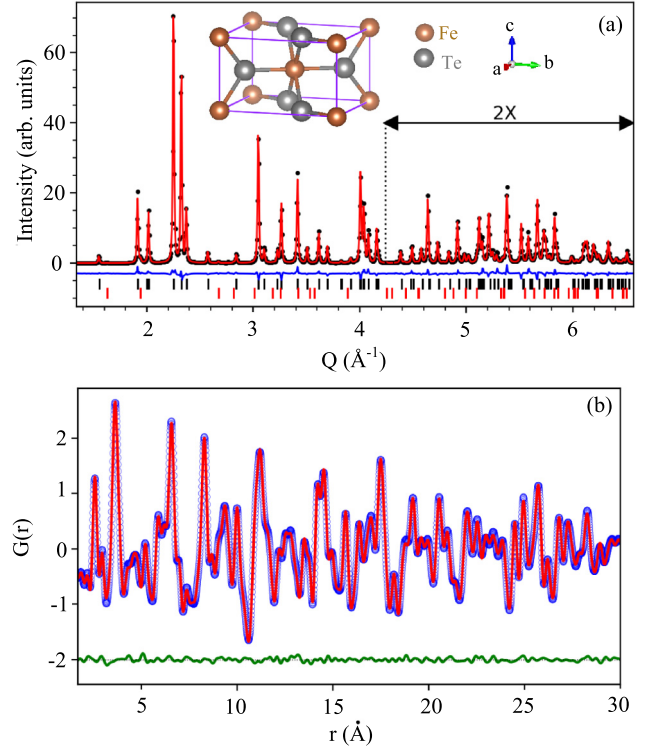


FIG. 1. (a) The Rietveld refinement of the background subtracted iron ditelluride synchrotron powder x-ray diffraction up to $Q \sim 6.5 \text{ \AA}^{-1}$. Plots show the observed (dots) and calculated (red solid line) powder patterns with a difference curve. The black vertical tick marks represent Bragg reflections in the *Pnmm* space group, whereas the red tick marks represent Bragg reflections of the small amount (0.6 t %) of residual Te on the crystal surface during pulverization of the single-crystal specimen. The inset shows the crystal structure of FeTe₂ in the *Pnmm* space group; the unit cell consists of $2 \times \text{Fe}_2$. (b) PDF analysis of Fe_{0.88(4)}Te₂. The PDF model (red solid line) is applied to observed data (open circles) at 300 K up to $r = 30 \text{ \AA}$. The difference curve is shown displaced below (green solid line).

finned against the experimental data. The unit cell parameters, a polynomial background function, fractional coordinates, isotropic atomic displacement parameters, and the overall scale parameter were refined sequentially to obtain the best fit ($R_w = 5\%$) [Fig. 1(a)]. Rietveld refinement indicates about 91(1)% occupancy at the $2/m$ atomic site of Fe with displacement parameters U_{eq} of $0.0055(1) \text{ \AA}^{-2}$ (Table III). Refinement also indicates 0.6 wt % of pure Te in the sample from the residual flux on the crystal surface. The FeTe₂ crystal structure features a Fe atom in the crystal lattice surrounded octahedrally by six chalcogen atoms which form hybrid d^2sp^3 bonds

TABLE III. Atomic coordinates and displacements parameters (Å²) for Fe_{1- δ} Te₂ from Rietveld refinement of flux-grown crystals measured at 300 K in the synchrotron powder x-ray experiment.

Atom	occupancy	<i>x</i>	<i>y</i>	<i>z</i>	U_{eq}
Fe	0.912(7)	0	0	0	0.0055(13)
Te	1.000	0.22096(16)	0.36117(15)	0	0.00439

[Fig. 1(a), inset]. Two neighboring coordination octahedra share an edge, while one Te atom has a tetrahedral neighborhood and is bonded to three iron atoms and one Te atom [6,7].

Figure 1(b) shows the PDF fit resulting from the two-phase long-range order structural model obtained from Rietveld refinement ($R_w = 5.5\%$). The PDF model confirms the existence of 0.6 wt % of pure Te. However, the PDF analysis suggests $\sim 84(1)\%$ occupancy at the $2/m$ atomic site occupied by Fe with displacement parameters very similar to the Rietveld model [$0.005(2) \text{ \AA}^{-2}$]. If we assume full occupancy at the Fe site, R_w of both Rietveld and PDF fits increase ($\sim 8\%$). In general, missing Bragg intensities originating from occupational and/or any other sort of disorder give rise to diffuse scattering under the Bragg peaks. However, diffuse scattering is subtracted during the Rietveld refinement as part of the background. PDF analysis takes both Bragg and diffuse scatterings into account, and hence, the Fe site occupancy obtained from the PDF analysis should be more representative of the bulk. Most importantly, both methods confirm the partial occupancy of the Fe site, and therefore, we use $\text{Fe}_{1-\delta}\text{Te}_2$ in the analysis below.

Heat capacity [Fig. 2(a)] at high temperature approaches the Dulong-Petit value of $3NR$, where $N = 3$ is the atomic number in the chemical formula and R is the universal gas constant, $8.314 \text{ J mol}^{-1} \text{ K}^{-1}$. From the fit using $C_p/T = \gamma + \beta_3 T^2 + \beta_5 T^4$ at low temperature [inset in Fig. 3(a)], the linear coefficient of specific heat γ is $7.40(5) \text{ mJ mol}^{-1} \text{ K}^{-2}$, $\beta_5 = 6.46(2) \times 10^{-4} \text{ mJ mol}^{-1} \text{ K}^{-6}$. From $\beta_3 = 0.01(2) \text{ mJ mol}^{-1} \text{ K}^{-4}$, the Debye temperature is $\Theta_D = (12\pi^4 NR/5\beta_3)^{1/3} = 185.6(7) \text{ K}$.

Thermopower S is positive in the measured temperature range [Fig. 2(b)], consistent with the hole-type majority of carriers. The S value increases with increasing temperature. At 300 K, S is about $65 \mu\text{V/K}$, close to the polycrystal [12,34], pointing to the absence of phonon-drag effects. Thermal conductivity κ [Fig. 2(c)] is about two orders of magnitude smaller when compared to FeSb_2 marcasite and shows little change in a 9 T magnetic field, consistent with a dominant phonon contribution. The $\kappa(T)$ values below room temperature are very small and are comparable to high-performance thermoelectric materials [35,36]. Resistivity [Fig. 3(d)] for current applied along the b axis is featureless, which is typical for a bad metal, and shows little change.

Figures 2(e) and 2(f) show the dc magnetic susceptibility $\chi(T) = M/H$ of the $\text{Fe}_{1-\delta}\text{Te}_2$ single crystal for $H = 1000 \text{ Oe}$ applied for both CVT- and flux-grown crystals. The CVT-grown crystals have much higher values of $\chi(T)$ in the whole measurement range. Removal of the crystal surface results in reduced susceptibility values, particularly at lower temperatures. This indicates a higher contribution of extrinsic impurities such as elemental Fe or Fe halides that did not react with Te in the CVT synthesis process. For flux-grown crystals, all $\chi(T)$ curves indicate paramagnetic behavior and can be fitted by the Curie-Weiss law: $\chi(T) = C/(T - \theta)$, where $C = N\mu_{\text{eff}}^2/3k_B$ is the Curie constant and θ is the Curie-Weiss temperature [Figs. 2(f) and 2(g)]. Fitted values for θ and effective moment μ_{eff} are $\theta_a = 288(6) \text{ K}$, $\mu_{\text{eff}a}/\mu_B = 0.27(1)$; $\theta_b = 284(5) \text{ K}$, $\mu_{\text{eff}b}/\mu_B = 0.34(1)$; and $\theta_c = 252(6) \text{ K}$, $\mu_{\text{eff}c}/\mu_B = 0.27(1)$ for magnetic field applied along the a , b , and c crystallographic axes, respectively. Positive θ values

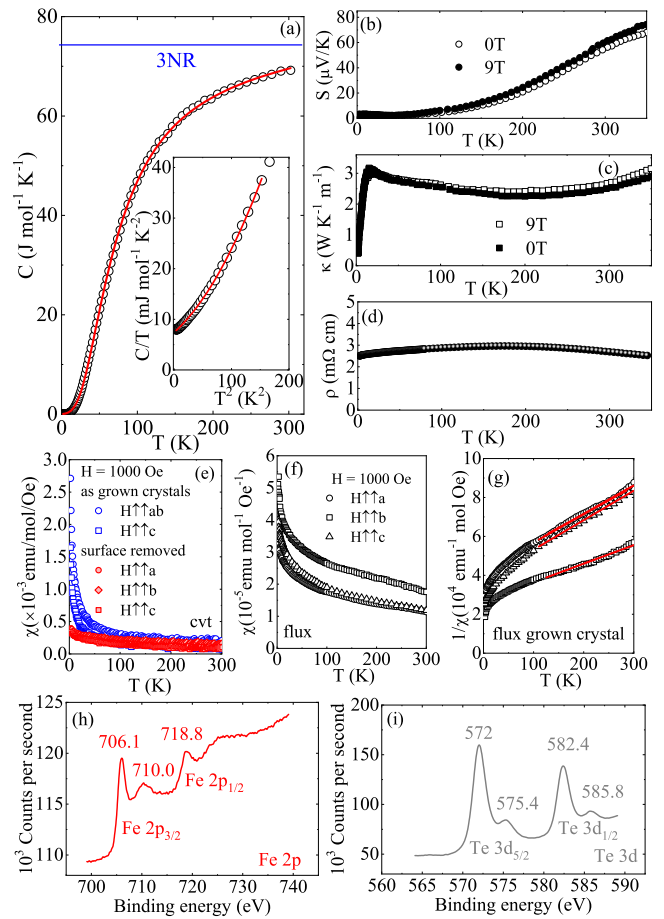


FIG. 2. (a) Temperature dependence of the heat capacity. The inset shows the low-temperature fit to $C/T = \gamma + \beta_3 T^2 + \beta_5 T^4$. (b) Thermopower $S(T)$, (c) thermal conductivity $\kappa(T)$, and (d) resistivity $\rho(T)$ for $\text{Fe}_{1-\delta}\text{Te}_2$ single crystals. (e)–(g) Magnetic susceptibility χ taken in $H = 1 \text{ kOe}$ magnetic field. (h) and (i) XPS Fe 2p and Te 3d peaks.

indicate dominant ferromagnetic interactions. The major Fe 2p and Te 3d peaks in XPS analysis [Figs. 2(h) and 2(i)] suggest a dominant metallic state, which indicates substantial hybridization of Fe orbitals [37–41].

Room temperature reflectance for the light polarizations along the a and b axes is shown in the main panel of Fig. 3(a), and that for the unpolarized light is shown in the inset. First, we note that reflectance increases rapidly, reaching above 80% toward low frequencies, consistent with the presence of free carriers. Second, there are several sharp features, at energies between 0.12 eV (968 cm^{-1}) and 0.4 eV (3226 cm^{-1}). We have not performed lattice vibration calculations for this study, but these energies are significantly above those expected from phonon modes. We propose here that they are associated with intraband and interband transitions, suggesting a complex electronic band structure, as we will discuss below. Last, as can be seen from the main panel, reflectance shows low, but noticeable, anisotropy between the two polarizations for almost the entire measured range.

Figure 3(b) displays the real part of optical conductivity $\sigma_1(\omega)$ for both for polarized (main panel) and

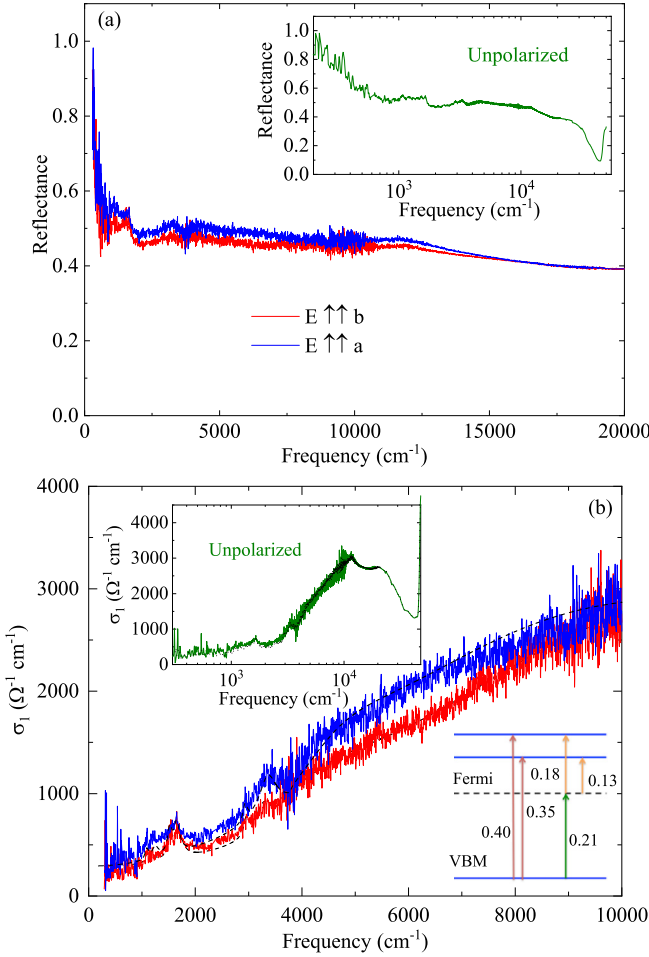


FIG. 3. (a) Reflectance for two different polarizations and unpolarized light (inset). (b). Optical conductivity for polarized (main panel) and unpolarized (left inset) radiation obtained from Kramers-Kronig transformations. The right inset shows a sketch of the energy levels involved in optical transitions (in eV; see the text). Dashed and dotted black lines represent Lorentz-Drude fits for both the unpolarized (inset) and polarized (main panel) conductivities.

unpolarized (upper inset) radiation, obtained from Kramers-Kronig transformations. Like for reflectance, there is a finite, albeit low, zero-frequency (dc) conductivity; several weak, but sharp, features above 0.12 eV; and strong absorptions at higher energies, with onset around 0.40 eV. Anisotropy between the two polarizations is also observed in the main panel, and for a more detailed analysis, we fit $\sigma_1(\omega)$ with a Lorentz-Drude model, including a band gap transition. For the Drude (free) carriers we found a small difference between the two polarizations. This could be explained by assuming the same plasma frequency for both $\omega_p = 1.32 \pm 0.03$ eV and a difference in scattering rate $1/\tau$ of about 14% ($1/\tau \approx 0.8$ eV for $\vec{E} \uparrow\uparrow x$ and $1/\tau \approx 0.7$ eV for $\vec{E} \uparrow\uparrow y$). Thus, dc conductivity was found to be $\sigma_1(0) \approx 370 \Omega^{-1} \text{ cm}^{-1}$ when electric field $\vec{E} \uparrow\uparrow x$ axis and $\sigma_1(0) \approx 290 \Omega^{-1} \text{ cm}^{-1}$ for $\vec{E} \uparrow\uparrow y$ axis. These values are in good agreement with electrical resistivity data from Fig. 2(d), where $\sigma_1(0) \approx 400 \Omega^{-1} \text{ cm}^{-1}$. For the band gap transitions, we found $E_g \approx$

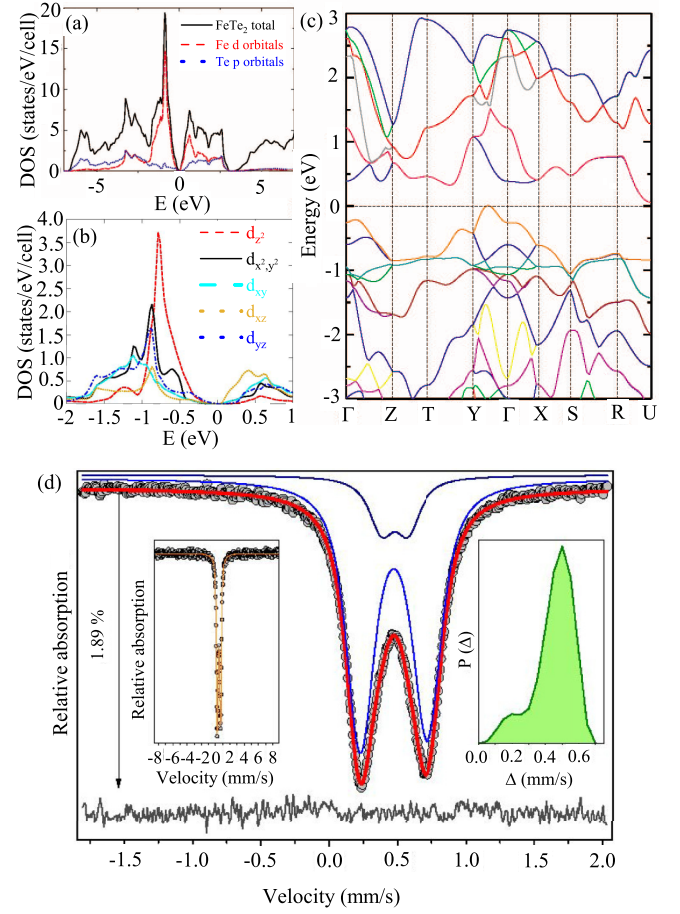


FIG. 4. (a) Total and atom-projected electronic densities of states for FeTe₂. (b) Projected density of states of Fe 3d orbital states in the vicinity of the Fermi level. (c) Calculated GGA band structure for FeTe₂. (d) Mössbauer spectrum recorded within the low-velocity range at room temperature. The observed data are presented by the gray solid circles, the fit is given by the red solid line, and the difference ($I_{\text{calc}} - I_{\text{obs}}$) is shown by the dark gray line. The QSDs obtained with the VBF method are depicted by the blue and navy blue lines. The vertical arrow denotes the relative position of the lowest experimental point with respect to the background (relative absorption of 1.89%). The absolute difference is less than 0.054%. The inset on the left side shows the spectrum recorded within the high-velocity range as evidence that there is no magnetic phase in the sample at room temperature. The orange line is just a guide for the eye. The inset on the right side shows the QSD calculated using the histogram method.

0.42 eV for $\vec{E} \uparrow\uparrow x$ axis and $E_g \approx 0.47$ eV $\vec{E} \uparrow\uparrow y$ axis. In a simple semiconductor picture, there should be no absorptions below the band gap, other than phonon vibrations and a Drude band. As phonons are expected at much lower energies and the Drude conductivity manifests as a continuous, broad band, we propose here the following explanation for the additional absorptions. Recent band structure calculations found that exchange spin splitting, crystal field and electron correlations, produces spin splitting of the e_g and t_g orbitals of the Fe 3d shell, giving rise to a band structure at the high-symmetry point, similar to the sketch in the lower inset of Fig. 4(b) [42].

Within such a picture of the energy levels, we determine the energies (in eV) for each transition based on the position of the sharp, narrow absorption peaks from Fig. 3(b).

For better understanding of defects [Fig. 1(c)], we calculated the $2 \times 2 \times 2$ supercells of FeTe_2 with one and two vacancies on the Fe site V_{Fe} and with one vacancy on the Te site V_{Te} . The Monkhorst-Pack scheme of the k points [43] of the BZ of the supercells was reduced to the $3 \times 2 \times 4$ grid. The atomic positions within the supercells were relaxed. Since the orthorhombic FeTe_2 covers the narrow area of the Fe-Te phase diagram, we also performed the density functional theory calculations of the hyperfine interaction (HFI) parameters of ^{57}Fe , which substitute the Te ion in tellurium with the hexagonal $P3_121$ (152) space group. The unit cell of the $P3_121$ tellurium consists of three inequivalent crystallographic sites. The calculation method was the same as in the previous calculations. The BZ sampling was done using $21 \times 21 \times 17$ and $7 \times 7 \times 5$ grids of k points for the unit cell and a $2 \times 2 \times 2$ supercell calculation. The crystal lattice parameters of the unit cell and all three atomic positions were optimized by minimization of the total energy and atomic forces. The calculated lattice parameters are $a = 0.46102$ nm and $c = 0.59671$ nm, in agreement with the experiment [44]. One of the eight equivalent tellurium atoms of the supercell was replaced with an iron atom for each of the three unequal tellurium sites in this calculation. The 24 atomic positions were relaxed in each calculation.

The total density of states (DOS) of FeTe_2 , along with the atom-projected Fe d and Te p DOSs, is presented in Figs. 4(a) and 4(b). The relatively narrow bands below and above the Fermi level E_F have primarily Fe $3d$ character with a small Te p contribution. The generalized gradient approximation (GGA) approximation indicates a relatively small DOS at E_F , in agreement with experimental results. When compared to FeSb_2 [45], the DOS at E_F is considerably smaller, while the overall shape of the DOS shows greater differences mainly in the unoccupied part. The band structure of FeTe_2 is presented in Fig. 4(c). The band gap is of the indirect type. The maximum of the valence band is located on the Y - G line, unlike the corresponding FeSb_2 maximum, which is located at the R point [46]. The position of the conduction band minimum lies at the U point, in contrast to the FeSb_2 maximum found along the G - Z line [46]. We note that higher charge transfer is expected in FeTe_2 when compared to FeSb_2 due to a larger electronegativity difference. This will make the recently proposed formation of infinite ladders of anion pairs along the c -axis direction in marcasite-type structures less likely [47].

The Mössbauer spectrum taken at room temperature confirms the absence of long-range magnetic order [Fig. 4(d)]. The high-velocity spectrum (left inset) shows the absence of the hyperfine magnetic splitting. Similar asymmetric doublets were obtained from the polycrystalline FeTe_2 [48]; slowly cooled and annealed FeTe_2 [49]; and quenched, reground, and annealed FeTe_2 [50]. Differences among the published HFI parameters of the doublet were explained by the synthetic route, crystallization, particle size, and thermal history distinctions [48]. The Fe coordination polyhedron in $Pnm\bar{m}$ FeTe_2 is the irregular Te_6 octahedron. The Fe site symmetry is D_{2h} , and therefore, orbitals are split into twofold-degenerate ($d_{x^2-y^2}$, $d_{x^2-y^2}$) $3e_g$ orbitals and nondegenerate (d_{xy} , d_{yz} , and d_{xz}) b_{1g} +

TABLE IV. Fitted Mössbauer hyperfine parameters at 294 K for FeTe_2 . The relative subspectrum A , average central shift $\langle \delta \rangle$, average value of QSDs $\langle \Delta \rangle$, standard deviation of QSDs σ_Δ , and QSD skewness $\text{skew}(\langle \Delta \rangle)$ are given. The ^{57}Fe calculated hyperfine values at 0 K for FeTe_2 , $1V_{\text{Fe}}$ in $\text{Fe}_{16}\text{Te}_{32}$, and $1V_{\text{Te}}$ in $\text{Fe}_{16}\text{Te}_{32}$: $\Delta_{\text{calc}}^{\text{pure}} = 0.524$ mm s $^{-1}$ is the calculated quadrupole splitting value in the absence of vacancy. $\langle \Delta_{\text{calc}} \rangle$ is the average value of the calculated quadrupole splitting values, 0.438 for $1V_{\text{Fe}}$ in $\text{Fe}_{16}\text{Te}_{32}$ and 0.542 for $1V_{\text{Te}}$ in $\text{Fe}_{16}\text{Te}_{32}$. The standard deviation of the quadrupole splitting values $\sigma_{\Delta_{\text{calc}}}$ is 0.086 for $1V_{\text{Fe}}$ in $\text{Fe}_{16}\text{Te}_{32}$ and 0.267 for $1V_{\text{Te}}$ in $\text{Fe}_{16}\text{Te}_{32}$.

A (%)	$\langle \delta \rangle$ (mm s $^{-1}$)	$\langle \Delta \rangle$ (mm s $^{-1}$)	σ_Δ (mm s $^{-1}$)	$\text{skew}(\langle \Delta \rangle)$
85	0.468	0.493	0.100	0
15	0.475	0.194	0.059	0.008

$b_{2g} + b_{3g}$ electronic states [51]. The Fe $3d$ states are localized at the top of the valence band, hybridizing with the Te $5p$ states [11,13]. Hence, a doublet is expected in Mössbauer spectra in the absence of magnetic order. HFI calculations indicate that the largest component of the diagonalized tensor of the electric field gradient $V_{zz} = -3.0382 \times 10^{21}$ Vm $^{-2}$ and the asymmetry parameter $\eta = |(V_{yy} - V_{xx})/V_{zz}| = 0.4731$ for the iron atom at 0 K. The well-known expression for Δ in the ^{57}Fe Mössbauer spectroscopy ($\Delta_{\text{calc}} = 0.5eQ|V_{zz}|\sqrt{1 + \eta^2/3}$, $Q(^{57}\text{Fe}) = 0.16$ barn [52]) yields the Δ_{calc} value which is presented in Table IV.

Previous studies indicated the Goldanskii-Karyagin effect, an anisotropy of the recoilless fraction [49] which resulted in an asymmetric doublet. Therefore, unimodal distribution of quadrupole splittings (QSDs) with non-null values of skewness and kurtosis of distribution is expected. The obtained QSD [Fig. 4(d), right inset] is not unimodal. To proceed,

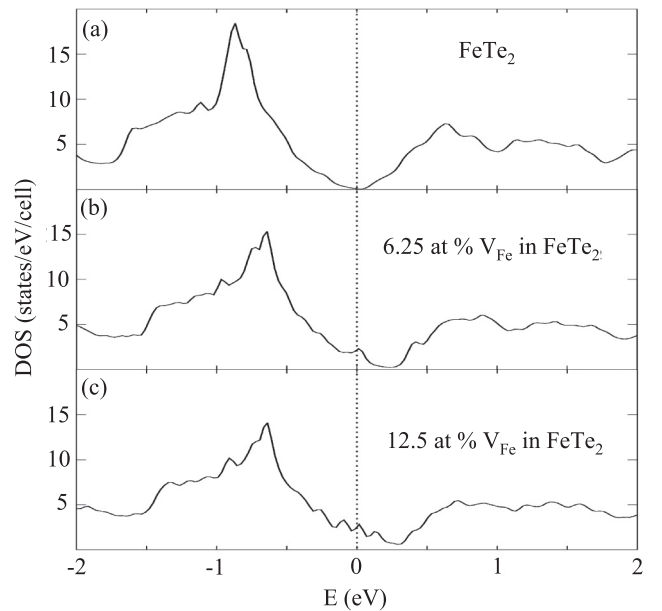


FIG. 5. Total DOS around the Fermi level in (a) pure $\text{FeTe}_{1-\delta}\text{Te}_2$, (b) the $2 \times 2 \times 2$ supercell with one Fe vacancy, and (c) the $2 \times 2 \times 2$ supercell with two Fe vacancies.

we applied the VBF two-doublet fitting model. The coupling parameters between the center shift δ and the quadrupole splitting Δ of the main doublet were included as the next linear function: $\delta = \delta_0 + \delta_1 \Delta$. The coupling parameter δ_1 of the additional doublet was fixed to zero. The ratio of spectral areas of the low-energy peak to the high-energy peak of the main doublet was obtained as $A_-/A_+ = 1.00(1)$, while it was fixed to 1 for the second doublet. The results of these QSDs are shown in Table IV.

Using HFI parameter calculations, we tested the possibility that the second doublet stems from the Fe-doped Te. They gave very similar Δ_{calc} values of $\approx 0.383 \text{ mm s}^{-1}$ at 0 K for all the three inequivalent iron positions. Assuming that the recoilless fractions for each of the inequivalent Fe sites have nearly the same values, the relative spectral area of 15% would yield about 5% of this phase. However, this is inconsistent with the powder x-ray result (Fig. 1).

Next, we examine the possibility for vacancy defects in FeTe_2 . The HFI calculations revealed that in both cases, V_{Fe} and V_{Te} , most tellurium ions around the vacancy move slightly toward the vacancy center. The V_{Te} (V_{Fe}) creation in the $2 \times 2 \times 2$ FeTe_2 supercell with a concentration of 1/32 (1/16) leads to the different Δ_{calc} values at all 16 (15) ^{57}Fe nuclei. The average values of the two performed HFI calculations for both cases are listed in Table IV. When one Te atom is missing, three octahedra are destroyed. A Δ_{calc} almost three times larger was calculated for the case of the Fe nucleus whose apical Te atom was removed compared to the case without vacancy ($\Delta_{\text{calc}}^{\text{pure}}$). The significant increase in Δ_{calc} is noted at the two Fe nuclei which have the vacancy at the basal position. In the other nuclei the Δ_{calc} values are 5%–25% less than $\Delta_{\text{calc}}^{\text{pure}}$. The smallest value of Δ_{calc} is found at the Fe nucleus whose apical Te ion is next to the vacancy center. The case of one iron atom vacancy shows different QSDs than the V_{Te} case. The smallest Δ_{calc} of 0.23 mms^{-1} is found at the Fe nucleus whose apical Te would bond to the missing Fe atom. A Δ_{calc} 5% lower than $\Delta_{\text{calc}}^{\text{pure}}$ is registered at the four atoms which would bridge the missing iron via the basal Te. The more susceptible Fe atoms are the four which would bridge the missing iron via the apical Te. Their Δ_{calc} are 30% smaller than $\Delta_{\text{calc}}^{\text{pure}}$. The two nuclei exhibit 7% greater Δ_{calc} values relative to $\Delta_{\text{calc}}^{\text{pure}}$. Their positions are well screened from the vacancy.

We tested several configurations in order to achieve 1/8 of V_{Fe} , whose difference in energies is less than 80 meV. The obtained values for Δ_{calc} at ^{57}Fe are within $0.123\text{--}0.593 \text{ mm s}^{-1}$, with an average value of 0.406 mm s^{-1} and a standard deviation of 0.122 mm s^{-1} . The skewness of this distribution is negative, pointing to a longer tail on the low-energy side, which resembles the measured bimodal distribution. The susceptibility of Δ_{calc} relative to the local lattice distortion is similar for both iron vacancy concentrations.

According to the HFI calculations, both types of vacancies could contribute to the low-energy side of the QSD. The prominent part of the QSD on the high-energy side in the case of V_{Te} is not registered in our Mössbauer spectrum. Hence, the iron atomic vacancies V_{Fe} in the sample cause the additional doublet in the spectrum. The tail right end of the QSD [right

inset in Fig. 4(d)] points to a nonuniform distribution of Fe vacancies in the lattice. Also, vacancies contribute to the main doublet through its Gaussian width. One V_{Fe} induces changes in Δ at several surrounding Fe nuclei, resulting in a relative spectral area of 15%, in approximate agreement with PDF refinement [Fig. 1(b)]. A_-/A_+ of the main doublet is 1.00(1), indicating the absence of the Goldanskii-Karyagin effect in $\text{Fe}_{1-\delta}\text{Te}_2$.

Several different pairs of iron vacancies have been investigated in order to examine the influence of atomic defects. The one shown in Fig. 5 corresponds to the removal of two next-nearest iron atoms at a distance of 4.53 Å, which is a combination that was found to have the lowest total energy. The GGA approximation predicts that iron vacancies should change the electronic structure of $\text{Fe}_{1-\delta}\text{Te}_2$ by providing additional states in the vicinity of the Fermi level. This leads to an increase of the DOS at the Fermi level. We also found an increase of the DOS with increased Fe vacancy concentration and a sizable shift of the main valence peak toward smaller energies.

IV. CONCLUSIONS

In summary, we have synthesized $\text{Fe}_{1-\delta}\text{Te}_2$ single crystals using two different synthesis methods, from Te flux and from CVT. Both types of crystals show Fe vacancy defects. In conjunction with EDX and single-crystal x-ray analysis, the results imply the width of formation of the marcasite structure for iron ditelluride and $\text{Fe}_{0.90(6)}\text{Te}_2$ stoichiometry, i.e., $\delta \approx 0.10(6)$, with the bulk value in flux-grown crystals being closer to $\delta \approx 0.15(1)$, whereas crystals made from CVT form with higher Fe content near the crystal surface. We observe the absence of long-range magnetic order, bad metal resistivity behavior with small anisotropy in the scattering rates, and very low thermal conductivity values. The defects do not change the symmetry of the crystallographic unit cell. Our study points to the importance of defects and calls for their evaluation in FeTe_2 ultrathin crystals [53] and other two-dimensional transition metal dichalcogenides.

ACKNOWLEDGMENTS

Work carried out at Brookhaven was supported by the U.S. Department of Energy, Basic Energy Sciences, Division of Materials Science and Engineering, under Contract No. DE-SC0012704 (BNL). J.T. acknowledges the support from a scholarship of the Faculty Training Abroad Program of Henan University. The research on local structures was funded by the Ministry of Education, Science and Technological Development of the Republic of Serbia. Single-crystal diffraction work carried out at the University of Delaware was supported by the U.S. Department of Energy, Office of Science, Basic Energy Sciences, under Award No. DE-SC0008885. This research used resources of the Center for Functional Nanomaterials (CFN), which is a U.S. DOE Office of Science Facility, at BNL under Contract No. DE-SC0012704.

[1] F. A. Rodin, M. Trushin, A. Carvalho, and A. H. Castro Neto, *Nat. Rev. Phys.* **2**, 524 (2020).

[2] J.-F. Dayen, S. Ray, O. Karis, I. J. Vera-Marun, and M. V. Kamalakar, *Appl. Phys. Rev.* **7**, 013303 (2020).

- [3] X. Chia and M. Pumera, *Nat. Catal.* **1**, 909 (2018).
- [4] X. Xie, M. Mao, S. Qi, and J. Ma, *CrystEngComm* **21**, 3755 (2019).
- [5] M. Long, P. Wang, H. Fang, and W. Hu, *Adv. Funct. Mater.* **29**, 1803807 (2019).
- [6] M. J. Buerger, *Z. Kristallogr.* **97**, 504 (1937).
- [7] F. Hulliger and E. Mooser, *J. Phys. Chem. Solids* **26**, 429 (1965).
- [8] I. Tsubokawa and S. Chiba, *J. Phys. Soc. Jpn.* **14**, 1120 (1959).
- [9] D. M. Finlayson, J. P. Llewellyn, and T. Smith, *Proc. Phys. Soc. London* **74**, 75 (1959).
- [10] A. Rahman, D. Zhang, M. U. Rehman, M. Zhang, X. Wang, R. Dai, Z. Wang, X. Tao, and Z. Zhang, *J. Phys.: Condens. Matter* **32**, 035808 (2020).
- [11] A. Ghosh and R. Thangavel, *Indian J. Phys.* **91**, 1339 (2017).
- [12] T. Harada, *J. Phys. Soc. Jpn.* **67**, 1352 (1998).
- [13] V. K. Gudelli, V. Kanchana, G. Vaitheeswaran, M. C. Valsakumar, and S. D. Mahanti, *RSC Adv.* **4**, 9424 (2014).
- [14] X. Sui, T. Hu, J. Wang, B.-L. Gu, W. Duan, and M.-s. Miao, *Phys. Rev. B* **96**, 041410(R) (2017).
- [15] M. Lan, G. Xiang, Y. Nie, D. Yang, and X. Zhang, *RSC Adv.* **6**, 31758 (2016).
- [16] C. Ataca, H. Sahin, and S. Ciraci, *J. Phys. Chem. C* **116**, 8983 (2012).
- [17] S. Chen, H. Liu, F. Chen, K. Zhou, and Y. Xue, *ACS Nano* **14**, 11473 (2020).
- [18] J. P. Llewellyn and T. Smith, *Proc. Phys. Soc. London* **74**, 65 (1959).
- [19] A. Walsh and A. Zunger, *Nat. Mater.* **16**, 964 (2017).
- [20] D. F. Bowman, E. Cemal, T. Lehner, A. R. Wildes, L. Mangin-Thro, G. J. Nilsen, M. J. Gutmann, D. J. Voneshen, D. Prabhakaran, A. T. Boothroyd, D. G. Porter, C. Castelnovo, K. Refson, and J. P. Goff, *Nat. Commun.* **10**, 637 (2019).
- [21] D. W. Boukhvalov and A. Politano, *Nanoscale* **12**, 20875 (2020).
- [22] H. Ipsier, K. L. Komarek, and H. Mikler, *Montash Chem.* **105**, 1322 (1974).
- [23] G. M. Sheldrick, *Acta Crystallogr., Sect. C* **71**, 3 (2015).
- [24] *International Tables for Crystallography*, 6th ed., edited by A. J. C. Wilson and E. Prince (Kluwer Academic, Norwell, MA, 1999), Vol. C, p. 548.
- [25] A. P. Hammersley, S. O. Svenson, M. Hanfland, and D. Hauserman, *High Pressure Res.* **14**, 235 (1996).
- [26] B. H. Toby, *J. Appl. Crystallogr.* **34**, 210 (2001).
- [27] C. L. Farrow, P. Juhas, J. W. Liu, D. Bryndin, E. S. Bozin, J. Bloch, T. Proffen, and S. J. L. Billinge, *J. Phys.: Condens. Matter* **19**, 335219 (2007).
- [28] D. G. Rancourt and J. Y. Ping, *Nucl. Instrum. Methods Phys. Res., Sect. B* **58**, 85 (1991).
- [29] R. A. Brand, *Winnormos Mössbauer Fitting Program*, Universität Duisburg (Duisburg, Germany, 2008).
- [30] P. Blaha, K. Schwarz, G. Madsen, D. Kvasnicka, and J. Luitz, Wien2k, *An Augmented Plane Wave + Local Orbitals Program for Calculating Crystal Properties*, edited by K. Schwarz (Technische Universität Wien, Vienna, 2001).
- [31] J. P. Perdew, K. Burke, and M. Ernzerhof, *Phys. Rev. Lett.* **77**, 3865 (1996).
- [32] P. E. Blöchl, O. Jepsen, and O. K. Andersen, *Phys. Rev. B* **49**, 16223 (1994).
- [33] Cambridge Crystallographic Database Centre depository numbers CSD 2115035 (Fe₂-f) and CSD 2115036 (Fe₂-c).
- [34] L. D. Dudkin and V. I. Vaidanich, *Sov. Phys. Solid State* **2**, 1384 (1961).
- [35] G. J. Snyder and E. S. Toberer, *Nat. Mater.* **7**, 105 (2008).
- [36] M. G. Kanatzidis, *Chem. Mater.* **22**, 648 (2010).
- [37] D. D. Hawn and B. M. DeKoven, *Surf. Interface Anal.* **10**, 63 (1987).
- [38] H. Konno and M. Nagayama, *J. Electron Spectrosc. Relat. Phenom.* **18**, 341 (1980).
- [39] J. M. Thomas, I. Adams, R. H. Williams, and M. Barber, *J. Chem. Soc., Faraday Trans. 2* **68**, 755 (1972).
- [40] M. K. Bahl and R. I. Watson, *J. Electron. Spectrosc. Relat. Phenom.* **10**, 111 (1977).
- [41] A. B. Mandale and S. Badrinarayanan, *J. Electron Spectrosc. Relat. Phenom.* **53**, 87 (1990).
- [42] L. Liang, S. Chen, Z. Lin, and X. Zhang, *Phys. Chem. Lett.* **11**, 7893 (2020).
- [43] H. J. Monkhorst and J. D. Pack, *Phys. Rev. B* **13**, 5188 (1976).
- [44] P. Cherin and P. Unger, *Acta Crystallogr.* **23**, 670 (1967).
- [45] A. Bentien, G. K. H. Madsen, S. Johnsen, and B. B. Iversen, *Phys. Rev. B* **74**, 205105 (2006).
- [46] A. V. Lukoyanov, V. V. Mazurenko, V. I. Anisimov, M. Sigrist, and T. M. Rice, *Eur. Phys. J. B* **53**, 205 (2006).
- [47] T. B. E. Grønbech, K. Tolborg, H. Svendsen, J. Overgaard, Y.-S. Chen, and B. B. Iversen, *Chem. Eur. J.* **26**, 8651 (2020).
- [48] Y. Xie, L. Zhu, X. Jiang, J. Lu, X. Zheng, W. He, and Y. Li, *Chem. Mater.* **13**, 3927 (2001).
- [49] K. V. Reddy and S. C. Chetty, *Phys. Status Solidi A* **37**, 687 (1976).
- [50] J. Stanek and P. Fornal, *Nukleonika* **49**, S63 (2004).
- [51] I. B. Bersuker, *Electronic Structure and Properties of Transition Metal Compounds: Introduction to the Theory* (Wiley, Hoboken, NJ, 2012).
- [52] P. Dufek, P. Blaha, and K. Schwarz, *Phys. Rev. Lett.* **75**, 3545 (1995).
- [53] D. Capitano, Z. Hu, Y. Liu, X. Tong, D. Nykypanchuk, D. DiMarzio, and C. Petrovic, *ACS Omega* **6**, 10537 (2021).